Chapter 6

Nonequilibrium effects for weak electron-phonon coupling

6.1 Introduction

The vision of molecular electronics [2] in part depends on the realization of devices such as molecular transistors, switches, or diodes. One strategy towards this goal involves the coupling of electronic and vibrational (phononic) degrees of freedom of molecules. A question of principal importance for single-molecule devices are the consequences of nonequilibrium effects at finite bias. Strong nonequilibrium molecular vibrations can be beneficial in molecular devices, e.g., by enhancing switching rates between molecular conformations. In other instances, they may hinder the operation of devices, in the extreme case by inducing dissociation of the molecule. Recent theoretical work – some of it included in this thesis – shows that even within simple models, vibrational nonequilibrium has important effects on IVs and shot noise [45, 59], may induce a shuttling instability [75, 76], or lead to current flow characterized by a self-similar hierarchy of avalanches of large numbers of transferred electrons (see Chapters 3 and 4).

Recent numerical results by Mitra et al. [45] suggest that intriguingly, vibrational nonequilibrium becomes stronger as the electron-phonon coupling λ *decreases*. Characterizing the vibrational nonequilibrium by the probability distribution of phonon excitations, these authors observe that the width of this distribution grows with decreasing coupling λ. These numerical results are obtained within a minimal model describing transport through one molecular orbital, which is coupled to a single vibrational mode (Anderson-Holstein model).

In this chapter,[1] we first clarify the underlying mechanism for this nonequilibrium effect by developing an analytical theory. Our approach relies on a mapping to a Fokker-Planck equation, which becomes exact in the limit of weak electron-phonon coupling. This mapping predicts that the width at half maximum (WHM) of the phonon distribution diverges as $\lambda \to 0$. Remarkably, the WHM is shown to scale as $\lambda^{-\alpha}$ with bias-dependent, non-integer exponents $\alpha > 0$. We confirm our analytical results by numerical simulations.

Real single-molecule devices will typically involve features such as several vibrational

[1] The research presented in this chapter is a result of a close collaboration in particular with M. Semmelhack.

modes, anharmonic vibrational potentials, and direct vibrational relaxation (e.g. due to radiation or interaction with the substrate), which are not fully captured by the Anderson-Holstein model. We therefore discuss how various such extensions of this model, which may be important for an accurate description of experimental systems, modify our analytical findings. Specifically, we include anharmonic vibrations within a Morse-potential model which allows us to discuss current-induced dissociation of the molecule. In this context, we show that the current-induced dissociation rate is governed by an interplay of the above-mentioned divergence of the width of the phonon distribution and a slowing down of the diffusion in phonon space as λ decreases.

The outline of the chapter is as follows: In Sec. 6.2 we discuss the nonequilibrium effects of weak electron-phonon coupling within the Anderson-Holstein model. This model was specified in Chapter 1, and the resulting properties of the phonon distribution for weak electron-phonon coupling are derived in Section 6.2. Nonequilibrium properties of real molecules are discussed in Sec. 6.3 by going beyond the Anderson-Holstein model. In particular, we address the effects of vibrational relaxation and the presence of several phonon modes as well as the situation of anharmonic potentials. Our conclusions are summarized in Sec. 6.4.

6.2 Weak electron-phonon coupling within the Anderson-Holstein model

Our starting point for the analysis of the weak electron-phonon coupling regime is the Anderson-Holstein Hamiltonian introduced in Chapter 1. We focus on the regime of strong Coulomb blockade, appropriate when voltage and temperature are small compared to the charging energy U. For simplicity, we assume a symmetric device with $\Gamma_L = \Gamma_R$ and identical voltage drops of $V/2$ across each junction.[2]

6.2.1 Phonon distributions for weak electron-phonon coupling

For $\lambda \ll 1$, the FC matrix elements [Eq. (2.3)] have the asymptotic behavior

$$|M_{q_1 q_2}|^2 \simeq \frac{Q!}{q!} \frac{\lambda^{2\Delta q}}{(\Delta q!)^2}, \tag{6.1}$$

valid for $q\lambda^2, \Delta q \lambda^2 \ll 1$, where $Q = \max\{q_1, q_2\}$, $q = \min\{q_1, q_2\}$, and $\Delta q = Q - q$. Therefore, the FC matrix elements and the transition rates $W_{qq'}^{n,n\pm1}$ decay rapidly with increasing Δq. Consequently, the vibrational state of the molecule is predominantly changed by processes for which $q \to q' = q \pm 1$, and $\Delta q = 1$. Neglecting all other processes, the rate equations describe a random walk in the space of phonon states q with q-dependent nearest-neighbor hopping rates. In this approximation, the random walker would eventually escape to infinity, as the rates for $q \rightleftharpoons q+1$ are equal and grow with q. This implies that there is *no steady-state* phonon distribution $P_q = \sum_n P_q^n$ within this random-walk model.

To derive the actual steady-state phonon distribution, it is therefore imperative to go beyond the random-walk model by including higher-order processes with $\Delta q > 1$. These

[2] We emphasize that our assumption of a symmetric device is not crucial for our essential results. Specifically, the scaling behavior, Eq. (6.3), is not sensitive to asymmetries of the molecule-lead coupling.

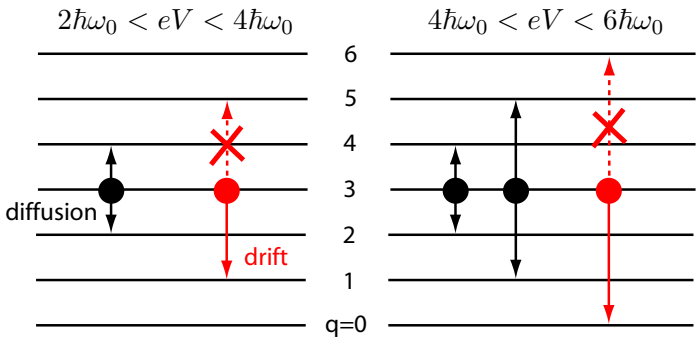

Figure 6.1: Illustration of the two process types determining the phonon dynamics: Phonon diffusion and phonon drift. The drift term originates from the fact that bias voltage limits the maximum phonon increase to $\lfloor eV/2\hbar\omega_0 \rfloor$. Larger changes of the phonon occupation are only possible for de-excitation processes.

may favor vibrational de-excitation processes since the applied voltage sets an upper limit to the increase (but not to the decrease!) in the vibrational excitation q by a tunneling event. For example, for $\varepsilon_d = 0$ the full voltage drop $eV/2$ per sequential-tunneling event can be converted into vibrational energy. Thus, $\Delta q_a = \lfloor eV/2\hbar\omega_0 \rfloor + 1$ is the leading-order asymmetric process *for which only de-excitation processes are permitted*. This situation is illustrated in Fig. 6.1.

We can now derive the scaling of the steady-state phonon distribution P_q with electron-phonon coupling λ by balancing the diffusion process due to tunneling events with $\Delta q = 1$ [with diffusion constant $\sim q\lambda^2$, see Eq. (6.1)] and the leading asymmetric drift process [with rate $(q\lambda^2)^{\Delta q_a}$, see Eq. (6.1)]. This leads to the balance equation

$$q\lambda^2 P_q'' \sim (q\lambda^2)^{\Delta q_a} P_q', \tag{6.2}$$

which implies a scaling law for the width q_0 of P_q, namely

$$q_0 \sim \lambda^{-\alpha}, \qquad \alpha = 2(\Delta q_a - 1)/\Delta q_a. \tag{6.3}$$

This power-law scaling is nicely confirmed by numerical results for P_q as shown in Fig. 6.2(a). Remarkably, for $k_BT \ll \hbar\omega_0$ the discrete dependence of the leading asymmetric process on bias and gate voltage implies finite regions in the (V, ε_d)-plane characterized by certain *non-integer* exponents α. The resulting "phase diagram" is shown in Figs. 6.2(b),(c) where the wedge-shaped regions A, B, and C correspond to $\alpha = 1, 4/3$, and $3/2$, respectively.[3]

For the diamond-shaped regions along the line $\varepsilon_d = 0$, marked in Fig. 6.2(b) by hatching, we can go beyond the derivation of this scaling behavior and obtain analytical results for the entire phonon distribution P_q by a mapping to a Fokker-Planck equation. The derivation exploits the crucial observation that for $U \to \infty$ and $k_BT \ll \hbar\omega_0$, the transition rates $W^{n\to n'}_{q\to q'} = s^{n\to n'} w_{q\to q'}$ factorize into a spin factor $s^{n\to n'} = (1 + \delta_{n',1})\delta_{|n-n'|,1}$ and a phonon factor

$$w_{q\to q'} = \tau_0^{-1} \left| M_{qq'} \right|^2 [\theta(q + \Delta q_a - 1 - q') + \theta(q - q' - \Delta q_a)], \tag{6.4}$$

[3] Additional smaller steps in Fig. 6.2(c) can be traced back to changes in the nature of the asymmetry within one scaling phase.

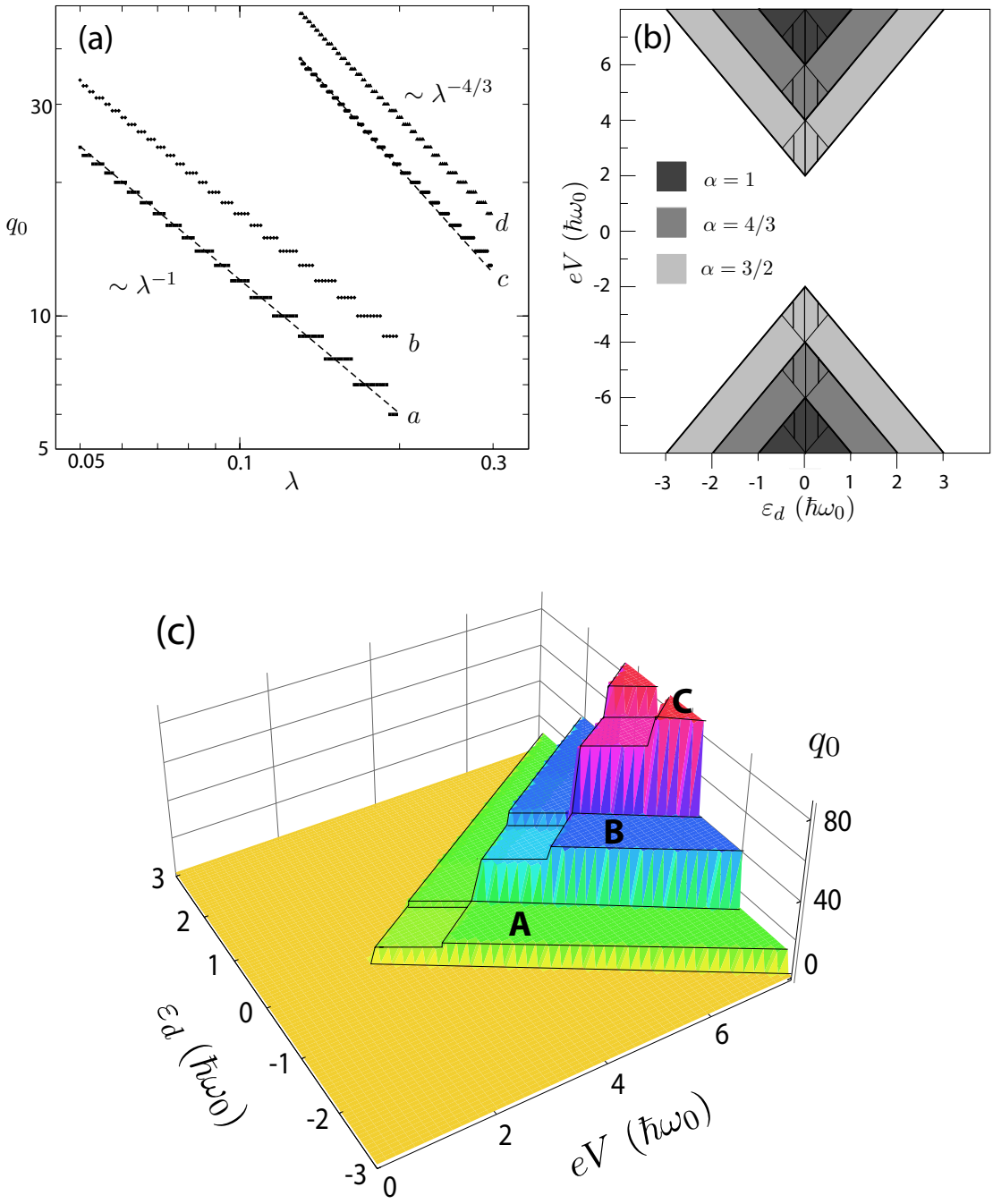

Figure 6.2: (a) Scaling behavior of the phonon distribution width as a function of electron-phonon coupling for representative values of $(eV/\hbar\omega_0, \varepsilon_d/\hbar\omega_0)$ equal to a: $(3,0)$; b: $(5,1)$; c: $(5,0)$; d: $(7,1)$. (b) Scaling domains as a function of bias and gate voltage. (c) Width of the phonon distribution as a function of bias and gate voltage at $\lambda = 0.15$ and $k_BT = 0.005\hbar\omega_0$. The scaling of the width differs for the plateaus according to A: $q_0 \sim \lambda^{-1}$, B: $q_0 \sim \lambda^{-4/3}$, and C: $q_0 \sim \lambda^{-3/2}$.

where $\tau_0^{-1} = \Gamma_a/\hbar = 2\pi\rho\,|t_a|^2/\hbar$. In the stationary case, this implies the factorization $P_q^n = P^n P_q$, which allows us to derive the *purely phononic* rate equation

$$0 = dP_q/dt = \sum_{q'} [P_{q'} w_{q'\to q} - P_q w_{q\to q'}], \tag{6.5}$$

Since the phonon distribution becomes wide, we can take q to be continuous, expand $P_{q'}$ around $q' = q$ up to second order, and keep only the leading-order contributions to diffusion and drift. In this way we obtain the Fokker-Planck equation

$$0 = \frac{\partial P}{\partial t} = \frac{1}{2}\frac{\partial^2}{\partial q^2}\left[D(q)P(q)\right] - \frac{\partial}{\partial q}\left[A(q)P(q)\right], \tag{6.6}$$

with diffusion coefficient $D(q) = 2q\lambda^2/\tau_0$, drift coefficient $A(q) = [\lambda^2 - c(q\lambda^2)^{\Delta q_a}]/\tau_0$, and $c = 2\Delta q_a(\Delta q_a!)^{-2}$. Remarkably, the stationary Fokker-Planck equation (6.6) can be solved analytically for any Δq_a by the scaling ansatz $P_q = a\lambda^\alpha f(\lambda^\alpha q)$ with a normalization constant a. The universal function f is uniquely determined by Eq. (6.6) together with the boundary conditions $f(0) = 1$, $f'(0) = 0$, and we find

$$f(x) = \exp\left[-x^{\Delta q_a}/b\right] \tag{6.7}$$

with $b = \frac{1}{2}(\Delta q_a!)^2$. Note that in particular, this analytical result confirms the power-law scaling (6.3) of the width of the phonon distribution. The power-law scaling (6.3) together with the analytical phonon distributions (6.7) constitute the central results of this chapter. The phonon distributions are nicely confirmed by numerical solutions of the full rate equations as shown in Fig. 6.3.[4]

In fully developed nonequilibrium, the width of the phonon distribution *diverges* with *decreasing* electron-phonon coupling λ, and the resulting phonon distributions are *non-analytic* in λ. An important theoretical implication of this result is that in fully developed nonequilibrium, perturbation theory in the electron-phonon coupling parameter λ is inadequate. Indeed, we find below that the radius of convergence of such an expansion in λ would involve the direct vibrational relaxation rate.

6.3 Implications for real molecules

Transport through real molecules will typically involve physics that goes beyond the Anderson-Holstein model. In particular, we will discuss

(i) direct vibrational relaxation,

(ii) the presence of more than one vibrational mode, and

(iii) anharmonic vibrational potentials.

We show that while the exact scaling results for phonon distributions are specific to the Anderson-Holstein model, nonequilibrium effects at weak electron-phonon coupling persist and can be understood within the phonon diffusion model as long as the vibrational relaxation rate remains small compared to I/e.

[4]The small deviations observed in the inset of Fig. 6.3(b) reflect that the effective perturbation parameter $q_0\lambda^2 \sim \lambda^{2/(\Delta q_a)}$ grows with Δq_a even at fixed λ.

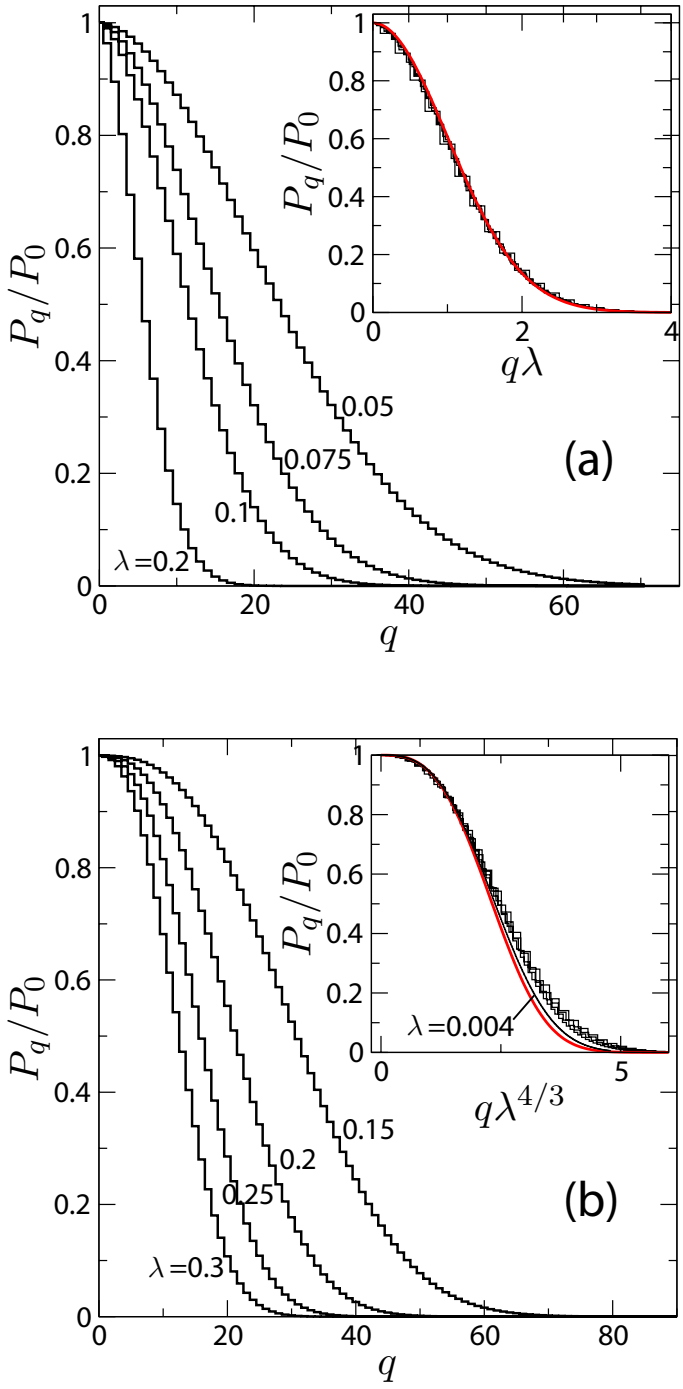

Figure 6.3: Phonon distributions P_q at bias voltages (a) $eV = 3\hbar\omega_0$ and (b) $eV = 5\hbar\omega_0$, plotted for several coupling strengths λ at $\varepsilon_d = 0$, $k_BT = 0.05\hbar\omega_0$. The insets show that these distributions (approximately) collapse to universal curves given by the red curves, which are the solutions of the the Fokker-Planck equation (6.6) specific to each voltage range $n\hbar\omega_0 < eV/2 < (n+1)\hbar\omega_0$.

6.3.1 Direct vibrational relaxation

Direct phonon relaxation can be included within the relaxation-time approximation by adding $-\frac{1}{\tau}[P_q^n - P_q^{\mathrm{eq}} \sum_{q'} P_{q'}^n]$ to the right-hand side of the rate equations, see Eq. (2.9). Here, P_q^{eq} denotes the equilibrium phonon distribution, which can be approximated by $P_q^{\mathrm{eq}} = \delta_{q,0}$ for $k_B T \ll \hbar\omega_0$.

To understand the effect of direct vibrational relaxation on the phonon distribution P_q, it is important to note that the diffusion and drift processes in phonon space slow down as the electron-phonon coupling λ decreases. As λ decreases, we therefore expect that there exists a crossover coupling λ_0: For $\lambda \gg \lambda_0$, the vibrational diffusion is limited by the drift in phonon space induced by the asymmetry between vibrational excitation and de-excitation, as discussed above. By contrast, for $\lambda \ll \lambda_0$ the dominant limiting process is direct vibrational relaxation, leading to a decrease of the width of the phonon distribution. This expectation is confirmed by numerical results as seen in Fig. 6.4(a) which shows the width of the phonon distribution as a function of λ for various relaxation rates. Fig. 6.4(b) shows the dependence of λ_0 on relaxation time τ for $\Delta q_a = 1$. Note that λ_0 grows only very slowly with increasing relaxation. While the λ_0 vs. τ dependence is close to a power law with an exponent 1/4 - 1/3, no simple scaling can be expected. The reason is that the scaling suggested by the rate equations amended by the relaxation term is incompatible with the scaling implied by the boundary condition $\lambda^{2(\alpha+1)} f'(0) = -\tau_0/\tau S a$ at $q = 0$, where $S = 1 + P^0$.

6.3.2 Additional vibrational modes

Typical molecules have many vibrational modes of different vibrational frequencies. We expect that the scenario discussed in this chapter is most relevant to molecules whose lowest frequency mode happens to be weakly coupled. As this mode becomes highly excited, it would start to mix with other (higher-frequency) modes. In the simplest approximation, we can account for such mode mixing as a channel of direct vibrational relaxation so that the discussion of the previous subsection applies. Indeed, due to this mixing, vibrational energy can be distributed among different modes, which will generally tend to decrease phonon occupation numbers, similar to the vibrational relaxation discussed above. Under these conditions, such a weakly coupled vibrational mode may provide an efficient pathway to "pump" higher-frequency vibrations.

6.3.3 Morse potential and dissociation

So far, our considerations were based on the harmonic approximation for the phonon potential. We argue however that wide phonon distributions are not an artefact of this approximation, but also appear for more realistic, anharmonic potentials. As an example, we investigate the effect of weak electron-phonon coupling for the Morse potential

$$V(x) = D\left[e^{-2\beta_m(x-x_0)} - 2e^{-\beta_m(x-x_0)}\right], \tag{6.8}$$

where $D > 0$ denotes the dissociation energy, β_m the inverse potential range, and x_0 the potential minimum position. The relevant basics of the Morse potential are reviewed in Appendix J.

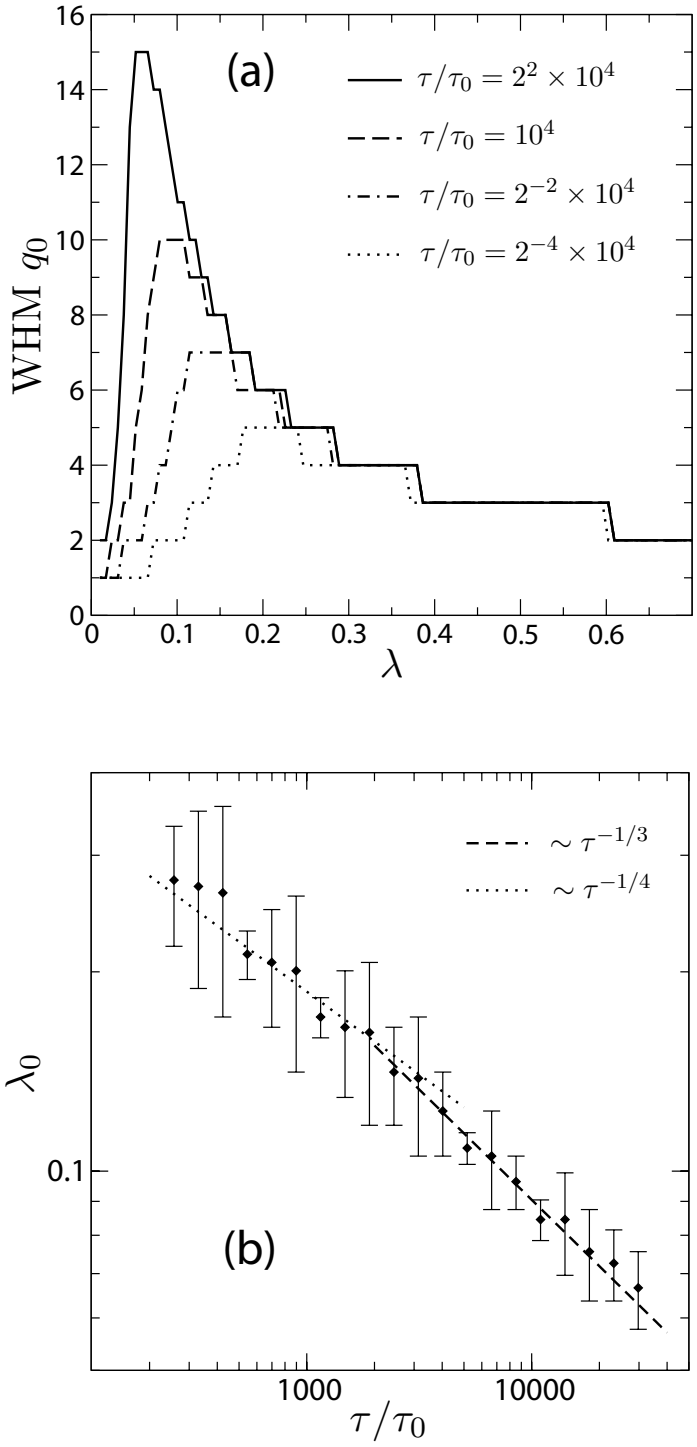

Figure 6.4: (a) Width of the phonon distribution as a function of electron-phonon coupling strength for several vibrational relaxation times τ and $eV = 3\hbar\omega_0$, $k_BT = 0.05\hbar\omega_0$, $\varepsilon_d = 0$. For $\lambda > 0.25$ all curves show the approximate $q_0 \sim \lambda^{-1}$ scaling. Below a relaxation-rate dependent crossover-point λ_0 the WHM is strongly suppressed due to direct relaxation. (b) Crossover-point λ_0 vs. relaxation time τ.

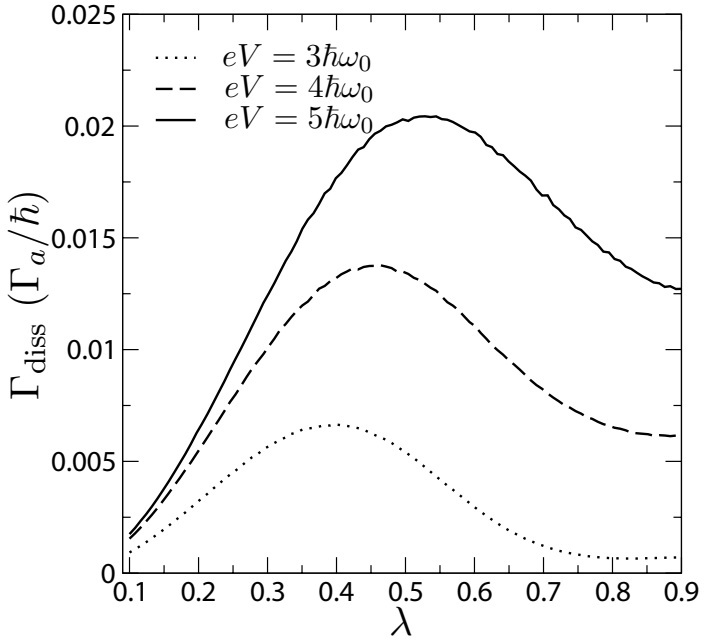

Figure 6.5: Mean dissociation rate as a function of electron-phonon coupling strength at $k_BT = 0.005\hbar\omega_0$ for several bias voltages as obtained by Monte Carlo simulation with a Morse potential containing 10 bound states.

The Morse potential [109] accurately describes the vibrations of diatomic molecules and allows us to study current-induced molecular dissociation [113]. This phenomenon has been explored experimentally in STM experiments with molecules on metal surfaces, and sufficiently high currents have been reported to lead to fast dissociation of the absorbed molecules [114]. While this scenario with strong coupling between the molecule and the metal surface is distinct from the regime addressed in this chapter, we remark that, in principle, the deposition of molecules on passivated surfaces [21] can be exploited to study the weak-coupling regime as well.

In analogy to the harmonic oscillator model, we assume that the potential energy curves for the neutral and singly-charged molecule have the same shape (i.e. D and β_m are fixed), but are shifted with respect to each other by $\Delta x = \sqrt{2}\lambda\ell_{\rm osc}$. Building on e.g. Ref. [115], we derive Franck-Condon matrix elements for the Morse potential between bound states as well as between bound and continuum states. Details of this calculation are contained in Appendix B.

Specifically, we study the current-induced dissociation rate of the molecule as function of electron-phonon coupling and bias voltage by Monte-Carlo simulation. Assuming low temperatures, and switching on the voltage at time $t = 0$, the molecule starts in the phonon ground state and then evolves in time due to the tunneling dynamics. Given that transitions from the continuum back to bound states are negligible, we obtain an average dissociation rate $\Gamma_{\rm diss}$ by recording the times $t_{{\rm diss},i}$ required for reaching the continuum and averaging over samples. (We note that calculations of mean first-passage times for the highest-lying bound level give compatible dissociation times.) Typical results for dissociation rates for

weak electron-phonon couplings (without relaxation) are depicted in Fig. 6.5.

The maximum in the dissociation rate $\Gamma_{\rm diss}$ vs. λ can be understood as a direct consequence of a competition between the broadening of the phonon distribution and the slowing down of diffusion in phonon space. As λ decreases from values of the order of unity, $\Gamma_{\rm diss}$ first increases. This reflects the concurrent increase in the width of the phonon distribution. Beyond the maximum, $\Gamma_{\rm diss}$ decreases due to the slowing down of diffusion in phonon space. Finally, the dissociation rate increases with voltage because of the increased width of the phonon distribution (see Fig. 6.2) and the possibility of multiple-phonon excitations within one tunneling event.

6.4 Conclusions

We have studied the current-induced vibrational nonequilibrium in single-molecule devices and found that remarkably, the width of the nonequilibrium phonon distribution increases with decreasing electron-phonon coupling. We have identified regions in the bias voltage-gate voltage plane in which the width of the phonon distribution exhibits power-law divergences with decreasing λ, with voltage-dependent noninteger exponents. In some representative cases, we are able to derive analytical phonon distributions by a mapping to a Fokker-Planck equation. These striking effects of current-induced nonequilibrium are found to have important implications in more realistic models which include direct vibrational relaxation and anharmonic potential surfaces. A very important conclusion from our work is that approaches which are perturbative in the electron-phonon coupling λ have to be assessed with extreme care in fully-developed nonequilibrium. Finally, we remark that recent experiments [44] show that the vibrational relaxation time can be as large as 10ns, in which case current-induced vibrational nonequilibrium becomes important for currents as small as 10pA.